

# Absolute Calibration and Characterization of the Multiband Imaging Photometer for Spitzer. III. An Asteroid-based Calibration of MIPS at $160\ \mu\text{m}$

J. A. Stansberry<sup>1</sup>, K.D. Gordon<sup>1</sup>, B. Bhattacharya<sup>2</sup>, C.W. Engelbracht<sup>1</sup>, G.H. Rieke<sup>1</sup>, F.R. Marleau<sup>2</sup>, D. Fadda<sup>2</sup>, D.T. Frayer<sup>2</sup>, A. Noriega-Crespo<sup>2</sup>, S. Wachter<sup>2</sup>, E.T. Young<sup>1</sup>, T.G. Müller<sup>3</sup>, D.M. Kelly<sup>1</sup>, M. Blaylock<sup>1</sup>, D. Henderson<sup>2</sup>, G. Neugebauer<sup>1</sup>, J.W. Beeman<sup>4</sup>, E.E. Haller<sup>4,5</sup>

## ABSTRACT

We describe the absolute calibration of the Multiband Imaging Photometer for Spitzer (MIPS)  $160\ \mu\text{m}$  channel. After the on-orbit discovery of a near-IR ghost image that dominates the signal for sources hotter than about 2000 K, we adopted a strategy utilizing asteroids to transfer the absolute calibrations of the MIPS 24 and  $70\ \mu\text{m}$  channels to the  $160\ \mu\text{m}$  channel. Near-simultaneous observations at all three wavelengths are taken, and photometry at the two shorter wavelengths is fit using the Standard Thermal Model. The  $160\ \mu\text{m}$  flux density is predicted from those fits and compared with the observed  $160\ \mu\text{m}$  signal to derive the conversion from instrumental units to surface brightness. The calibration factor we derive is  $41.7\ \text{MJy/sr/MIPS160}$  (MIPS160 being the instrumental units). The scatter in the individual measurements of the calibration factor, as well as an assesment of the external uncertainties inherent in the calibration, lead us to adopt an uncertainty of  $5.0\ \text{MJy/sr/MIPS160}$  (12%) for the absolute uncertainty on the  $160\ \mu\text{m}$  flux density of a particular source as determined from a single measurement. For sources brighter than about 2 Jy, non-linearity in the response of the  $160\ \mu\text{m}$  detectors produces an under-estimate of the flux density:

---

<sup>1</sup>Steward Observatory, University of Arizona, Tucson, AZ 85721

<sup>2</sup>Spitzer Science Center, 220-6, Caltech, Pasadena, CA 91125

<sup>3</sup>Max Planck Institute, D-85748 Garching, Germany

<sup>4</sup>Materials Science Division, Lawrence Berkeley National Lab, Berkeley, CA 94720

<sup>5</sup>Department of Materials Science and Engineering, University of California at Berkeley, Berkeley, CA 94720

for objects as bright as 4 Jy, measured flux densities are likely to be  $\simeq 20\%$  too low. This calibration has been checked against that of ISO (using ULIRGS) and IRAS (using IRAS-derived diameters), and is consistent with those at the 5% level.

## 1. Introduction

The Multiband Imaging Photometer for Spitzer (MIPS; Rieke et al. 2004) is the far-infrared imager on the Spitzer Space Telescope (*Spitzer*, Werner et al. 2004). MIPS has three photometric channels, at 24, 70, and 160  $\mu\text{m}$ . Like the other Spitzer instruments, the primary flux density calibrators at 24 and 70  $\mu\text{m}$  are stars. (IRAC: Reach et al. 2005; Fazio et al., 2004; Hora et al., 2004; and IRS: Houck et al., 2004). The calibration for the MIPS 24 and 70  $\mu\text{m}$  channels are presented in companion papers by Rieke et al. (2007), Engelbracht et al. (2007: 24  $\mu\text{m}$ ) and Gordon et al. (2007: 70  $\mu\text{m}$ ). Here we present the calibration of the 160  $\mu\text{m}$  channel, and describe some unexpected challenges that had to be overcome in performing the calibration. The emission from astronomical targets at this long wavelength is particularly useful in characterizing the abundance of cold dust, which frequently dominates the total emission from galaxies (e.g. Gordon et al., 2006; Dale et al., 2005). The MIPS 160  $\mu\text{m}$  channel has also contributed new insight into the sources responsible for the previously unresolved cosmic infrared background (Dole et al. 2006).

Very few calibrations exist in the 100–200  $\mu\text{m}$  wavelength regime. The Infrared Astronomical Satellite (IRAS; Neugebauer, 1984; Beichmann et al., 1985) 100  $\mu\text{m}$  channel, the 60 – 200  $\mu\text{m}$  channels of the ISO Imaging Photopolarimeter (ISOPHOT, Schulz et al. 2002) aboard the Infrared Space Observatory (ISO), and the Diffuse Infrared Background Explorer (DIRBE, at 60 to 240  $\mu\text{m}$ ; Hauser et al., 1998) aboard the Cosmic Infrared Background Explorer (COBE, e.g. Fixsen et al. 1997) relied on observations of solar system targets for their absolute calibrations. The Far Infrared Absolute Spectrophotometer (FIRAS) on COBE relied on observations of an external calibration target (Mather et al. 1999). In the case of IRAS, the calibration relied on observations of asteroids to extrapolate the calibration of the 60  $\mu\text{m}$  channel to 100  $\mu\text{m}$ . In the case of ISOPHOT, a few asteroids were studied in great detail, and their emission used as the basis of the absolute calibration (Müller and Lagerros, 1998; 2002). The primary reason these previous missions relied on observations of asteroids (and planets) to calibrate their longest-wavelength channels was sensitivity: the instruments could not detect enough stellar photospheres at adequate signal-to-noise ratio (SNR) over a wide-enough range of flux densities to support a calibration. In part that was because the instruments had large beams that were not well sampled by their detectors, leading to high

confusion limits to their sensitivity.

The original intention was to calibrate the MIPS  $160\ \mu\text{m}$  channel using observations and photospheric models of stars. Compared to the earlier missions, the MIPS detectors and electronics are significantly more sensitive. Also, the MIPS pixel scale,  $16''$ , fully samples the  $40''$  beam provided by *Spitzer*, resulting in lower confusion limits. After launch, the stellar calibration strategy was found to be unworkable because a bright, short-wavelength ghost image impinged on the array at nearly the same location as the  $160\ \mu\text{m}$  image (see below). The strategy we adopted was similar to that employed by IRAS: namely to use observations of asteroids in all three MIPS channels to transfer the calibration from the MIPS 24 and  $70\ \mu\text{m}$  channels to the  $160\ \mu\text{m}$  channel.

## 2. The Near-IR Ghost Image Problem

Initial  $160\ \mu\text{m}$  commissioning observations of stars seemed to indicate that the array was 10–15 times more responsive than expected from pre-launch models and instrument characterization tests. However, observations of cold sources seemed to confirm the expected responsivity of the array. Within 4 months of the launch of *Spitzer*, we concluded that for targets with stellar near-IR: $160\ \mu\text{m}$  colors, near-IR photons (with wavelengths  $\simeq 1.6\ \mu\text{m}$ ) were forming a ghost image on the  $160\ \mu\text{m}$  array.

The Ge detectors are sensitive to near-IR light because of their intrinsic photoconductive response. The desired response to  $160\ \mu\text{m}$  light, on the other hand, arises from the extrinsic photoconductive response (achieved by doping with Ga) coupled with mechanical stress applied to the pixels (which extends the response from the normal  $100\ \mu\text{m}$  cutoff to about  $200\ \mu\text{m}$ ). Optical modeling eventually indicated that near-IR photons diffusely reflected off the surface of the  $160\ \mu\text{m}$  short-wavelength blocking filter were responsible for the ghost image. That filter lies near an intermediate focus in the optical train, and the reflected photons form a poorly-focused ghost image on the array. By design, the blocking filter is tilted relative to the light path to prevent specularly reflected near-IR light from impinging on the array. However, roughness on the surface of the blocking filter contributes a diffuse component to the reflected near-IR light, and it is this diffusely reflected light that forms the ghost image.

The near-IR light reflected from the blocking filter passes through the  $160\ \mu\text{m}$  bandpass filter (which has transmission in the near-IR of about  $10^{-3}$ ), but does not pass through the blocking filter. As a result, the ghost image is quite bright in spite of the diffuse nature of the reflection, having an intensity 10–15 times greater than the intensity of the  $160\ \mu\text{m}$  image for

sources with stellar colors. The fact that the ghost image nearly coincides with the image of  $160\ \mu\text{m}$  light on the array (see Figure 1) made it difficult to identify the problem in the first place, and also makes it very difficult to calibrate the relative strengths of the two images. Their relative strengths also depend on the temperature of the source. For a blackbody source spectrum (and assuming that the effective wavelength of the ghost image is  $1.6\ \mu\text{m}$ ), objects with temperatures  $\geq 2000\ \text{K}$  will suffer from a ghost image comparable to or greater in brightness than the  $160\ \mu\text{m}$  image. Several attempts have been made to overcome these uncertainties and difficulties, and to characterize and calibrate the ghost-image directly, but have met with quite limited success.

### 3. Revised Calibration Strategy

Asteroids were chosen as the new calibrators because of their very red near-IR to  $160\ \mu\text{m}$  color, their ubiquity, and their range of brightness. For typical asteroids the brightness of the ghost image will be at least 2000 times fainter than the  $160\ \mu\text{m}$  image, and so will not measurably affect any calibration based on observations of asteroids. Unfortunately, asteroids also have several qualities that detract from their attraction as calibrators: their far-IR SEDs are difficult to predict (due to temperature variations across and within the surface), are time-variable (due to rotation and changing distance from the Sun and observer), and are poorly characterized at far-IR wavelengths. L and T dwarfs can not be used because they are far too faint to be detected using MIPS at  $160\ \mu\text{m}$ .

Because of the difficulty in predicting the  $160\ \mu\text{m}$  flux density from a given asteroid for a particular observing circumstance, we adopted a calibration strategy that relies on near-simultaneous observations of asteroids at 24, 70 and  $160\ \mu\text{m}$ , and then bootstraps the  $160\ \mu\text{m}$  calibration from the well-understood calibrations at 24 and  $70\ \mu\text{m}$ . Additionally, we have observed many asteroids, so that we can use the average properties of the data to derive the calibration, rather than relying on detailed efforts to model the thermal emission of individual asteroids. The emission from asteroids at wavelengths beyond  $60\ \mu\text{m}$  has only been characterized for a few objects (e.g. Müller and Lagerros, 1998; 2002), but those objects are all far too bright to observe with MIPS.

#### 3.1. Faint & Bright Samples

Because the far-IR SEDs of asteroids are not well studied, we felt that it was very important to characterize the thermal emission of our calibration targets at both 24 and  $70\ \mu\text{m}$  to

predict their emission at  $160\ \mu\text{m}$ . However, saturation limits introduce a complication in trying to observe any particular asteroid in all 3 MIPS channels. For a typical asteroid, the ratio of the flux densities,  $24:70:160\ \mu\text{m}$ , is about  $10:3:0.8$ . The  $24\ \mu\text{m}$  channel saturates at  $4.1\ \text{Jy}$  in 1 second, and somewhat brighter sources can be observed using the first-difference image, which has an exposure time of 0.5 seconds. This limits the maximum  $160\ \mu\text{m}$  brightness that can be related back to well-calibrated  $24\ \mu\text{m}$  observations to about  $0.5\ \text{Jy}$ . Sensitivity and confusion limits at  $160\ \mu\text{m}$  require that we observe asteroids brighter than about  $0.1\ \text{Jy}$  at  $160\ \mu\text{m}$ . Thus, the dynamic range of the  $160\ \mu\text{m}$  fluxes that can be directly tied to  $24\ \mu\text{m}$  observations is only a factor of 5, from  $100\ \text{mJy}$  to  $500\ \text{mJy}$ . The hard saturation limit at  $70\ \mu\text{m}$ ,  $23\ \text{Jy}$ , does not place any restriction on sources that can be observed at both  $70$  and  $160\ \mu\text{m}$  (the  $160\ \mu\text{m}$  saturation limit,  $3\ \text{Jy}$ , is about  $1/2$  of the  $160\ \mu\text{m}$  flux density from an asteroid with a  $23\ \text{Jy}$   $70\ \mu\text{m}$  brightness). These saturation-related restrictions lead us to adopt a 2-tiered observation and calibration strategy.

*Faint Asteroids:  $24\ \mu\text{m}$  sample.* We observe asteroids predicted to be fainter than  $\sim 4\ \text{Jy}$  at  $24\ \mu\text{m}$  in all three MIPS channels. The data are taken nearly simultaneously (typically less than 30 minutes to observe all 3 channels, with nearly all of that time being devoted to taking the  $160\ \mu\text{m}$  data). The short duration of the observations limits potential brightness variations due to rotation of the target (in addition, the targets were selected on the basis of not exhibiting strong visible lightcurve variations). We then use the observed flux densities at  $24$  and  $70\ \mu\text{m}$  to predict the flux density at  $160\ \mu\text{m}$  using a thermal model (see below). We also compute the ratio of the *measured*  $70\ \mu\text{m}$  flux density to the  $160\ \mu\text{m}$  *model prediction*, and use that ratio later to predict the  $160\ \mu\text{m}$  flux density for asteroids too bright to observe at  $24\ \mu\text{m}$ .

*Bright Asteroids:  $70\ \mu\text{m}$  sample.* For asteroids predicted to be brighter than  $\sim 4\ \text{Jy}$  at  $24\ \mu\text{m}$ , we observe only at  $70$  and  $160\ \mu\text{m}$ . We then use the average  $70:160$  color from the faint sample to predict the  $160\ \mu\text{m}$  flux density from the  $70\ \mu\text{m}$  observation. This sample extends the available dynamic range of the  $160\ \mu\text{m}$  observations by more than a factor of two relative to the  $24\ \mu\text{m}$  sample alone, allowing us to both measure the calibration factor up to the  $160\ \mu\text{m}$  saturation limit, and to determine whether the response is linear.

### 3.2. Limitations

This strategy is subject to some limitations in addition to uncertainties inherent to all absolute calibration schemes. The calibration we derive at  $160\ \mu\text{m}$  is wholly dependent on the MIPS calibrations at  $24$  and  $70\ \mu\text{m}$ , and its accuracy can not exceed the accuracy of the calibration of those channels. As described in Engelbracht et al. (2007), the absolute

calibration at  $24\ \mu\text{m}$  is good to 2%; Gordon et al. (2007) show that the  $70\ \mu\text{m}$  absolute calibration is good to 5.0%. These absolute calibration uncertainties in the shorter channels translate into a 7% uncertainty on the predicted  $160\ \mu\text{m}$  flux density of any object with a  $24:70\ \mu\text{m}$  color temperature of around 250 K (as our targets do). This represents the ultimate theoretical accuracy of the  $160\ \mu\text{m}$  calibration we can derive via the methods described here.

As mentioned above, the dynamic range of the  $160\ \mu\text{m}$  fluxes that we can relate to objects observed at both  $24$  and  $70\ \mu\text{m}$  is quite small. Thus, the bright sample is critical for extending the dynamic range of the calibration. However, our predicted  $160\ \mu\text{m}$  fluxes rely on the average  $70:160\ \mu\text{m}$  model color of the faint sample, so the calibration is dependent on the uncertainty in that color. The signal-to-noise ratio (SNR) of our measurements at the shorter wavelengths is typically in excess of 50, so their precision is not a major factor. However, the average  $70:160\ \mu\text{m}$  color we use depends on what we assume for the spectral emissivity of asteroids. There are hints in the ISO data that the emissivity of some asteroids is depressed by  $\simeq 10\%$  in the far-IR (Müller & Lagerros, 2002), and model-based predictions that surface roughness may also affect the slope of the far-IR thermal spectrum. Here we assume that asteroids emit as gray-bodies, and use a thermal model that does not incorporate the effect of surface roughness on the slope, and the calibration we derive follows directly from those assumption. The full impact of all of the uncertainties mentioned here on the accuracy of the calibration are discussed in § 8.1.

## 4. Observations and Data Analysis

### 4.1. The Observations

For each MIPS observing campaign, we used the JPL Solar System Dynamics division’s HORIZONS system (<http://ssd.jpl.nasa.gov>) to select main-belt asteroids within the Spitzer operational pointing zone. From this set, we selected objects with an albedo and diameter in the HORIZONS database (primarily derived from the IRAS asteroid catalog, Tedesco et al. 2002). For the purposes of observation planning only, we used the IRAS albedos and diameters to predict flux densities in the MIPS channels. We typically selected a few to observe, picking those that could be observed in a reasonable amount of time, would not saturate the detectors, and that did not have significant lightcurve amplitudes (again, as indicated by the HORIZONS database).

102 individual observations of asteroids were made through the 28th MIPS observing campaign (between December 2003 and January 2006). Of those, 79 resulted in  $160\ \mu\text{m}$  detections with signal-to-noise ratios  $\geq 4$ . Thirty-three of those were 3-color ( $24$ ,  $70$ , and

160  $\mu\text{m}$ ) observations of fainter asteroids, and 46 were 2-color (70 and 160  $\mu\text{m}$  only) of brighter objects. All observations were made using the MIPS photometry Astronomical Observing Template (AOT), which provides dithered images to improve point spread function (PSF) sampling and photometric repeatability. The 160  $\mu\text{m}$  array is quite small, having an (unfilled) instantaneous field of view (FOV) of 0.8 by 5.3 arcminutes. The photometry AOT, because of the dithers, results in a larger, but still restricted 2.1 by 6 arcminute filled FOV for the final mosaic. The diameter of the first Airy minimum of the 160  $\mu\text{m}$  PSF is 90". After collecting 160  $\mu\text{m}$  data using the standard dither pattern for a few observing campaigns, we began taking those data by combining the AOT with small map. This provided more sky around the target, and improved the sampling of the PSF. Figure 1 shows a sample 160  $\mu\text{m}$  image for a bright asteroid resulting from such an observation.

## 4.2. Data Analysis

The data were analyzed using the MIPS instrument team data analysis tools (DAT; Gordon et al., 2005). These tools have been used to develop the reduction algorithms and calibration of the MIPS data, beginning during ground-test, and continuing through on-orbit commissioning and routine operations. The Spitzer Science Center data processing pipeline is used to independently verify the algorithms and calibrations developed through the instrument team DAT. Both the SSC pipeline and the DAT use the same calibration files (e.g. darks, illumination corrections), and the same absolute calibration factors. Comparison of 160  $\mu\text{m}$  photometry for data processed through the DAT and the SSC pipeline show that the two agree to better than 1%. Data at 24 and 70  $\mu\text{m}$  were reduced, and photometry extracted, in exactly the same manner as all other calibration data for those channels (see Engelbracht et al. 2007, and Gordon et al. 2007). Because the exposure times at 24 and 70  $\mu\text{m}$  were so short, the motion of the asteroids during those observations was insignificant relative to the beam size in all cases. At 160  $\mu\text{m}$  the beam is typically much larger than target motion, even though the integration times in that channel were sometimes quite long. In the few instances where object motion during the 160  $\mu\text{m}$  observation was significant (160  $\mu\text{m}$  AOR execution times approaching one hour), we generated mosaics in the co-moving frame.

The basic processing of the 160  $\mu\text{m}$  data is described in Gordon et al. (2005). Briefly, each observation consists of multiple, dithered images. During acquisition of each image, termed a data collection event (DCE), the signal from the pixels is non-destructively sampled every 1/8 second. The pixels were reset every 40th sample. Cosmic rays are identified as discontinuities in the data ramps, and slopes are then fit to the cleaned ramps. Because the responsivity of the Ge:Ga array varies with time and flux-history, internal relative calibration

sources (stimulators) are flashed every 8th DCE during data collection. Each slope image is then ratioed to an (interpolated and background-subtracted) stimulator image, and the result corrected for the measured illumination pattern of the stimulators to produce a responsivity normalized image for each dither position in an observation. Those images are mosaicked using world coordinate system information to produce a final image of the sky and target. The mosaics used in this analysis were constructed using pixels  $8''$  square,  $\simeq 1/2$  the native pixel scale of the  $160\ \mu\text{m}$  array. This subsampling provides better PSF sampling and aids in identifying outlier pixels during mosaicking. Because the slope image from each DCE is ratioed to a stimulator image, brightness in the resulting mosaics is in dimensionless instrumental units which we will refer to as “MIPS160” units, or simply MIPS160. The goal of the calibration program is to derive the conversion (the “calibration factor,”  $CF$ ) between MIPS160 and surface brightness in units of, e.g., MJy/sr.

## 5. Photometry and Aperture Corrections

Figure 2 shows an azimuthally averaged radial profile of an observed  $160\ \mu\text{m}$  PSF, and compares it to model profiles generated using the Spitzer PSF software (STinyTim, v1.3; Krist, 2002). The measured profile is derived from the observation of the bright (2.3 Jy) asteroid Papagena (see Figure 1); other observations result in very similar PSFs. Model PSFs were generated assuming a source with a 250 K blackbody spectrum, consistent with the temperatures we find for our sample. The models were also generated using 5-times oversampling, resulting in model pixels  $3''.2$  square. As is seen for the other two MIPS channels (see Engelbracht et al., 2007, and Gordon et al. 2007), the primary difference between the model and observed PSFs is in the region of the first Airy minimum. However, suitably smoothed, the model PSF represents the observed PSF quite well. This is reflected in Figure 1, where the overall morphology of the observed and model PSFs can be compared. Figure 2 compares the radial profiles for the observed and model PSFs, and shows the good agreement between the two. The best-fit model PSF is smoothed using a boxcar with a width of  $25''.6$ , corresponding to a width of 1.6 native pixels.

Because of the restricted FOV of the  $160\ \mu\text{m}$  images, we are forced to use small apertures for performing photometry (this is in contrast to the large apertures used to derive the 24 and  $70\ \mu\text{m}$  calibrations). Thus the calibration at  $160\ \mu\text{m}$  depends more strongly on the aperture corrections. We computed aperture corrections based on the model PSF shown in Figures 1 and 2. The models offer two advantages over the observed PSF: they are noiseless, and there is no uncertainty associated with determining the background (particularly difficult at  $160\ \mu\text{m}$  because of the restricted FOV). The total flux in STinyTim model PSFs depends



on the model FOV: we utilized models  $128'$  across in order to capture most of the flux in the far-field of the PSF. We have extrapolated the PSF to  $512'$  using an Airy function, and integrated over that much larger model to constrain the magnitude of any bias in our aperture corrections stemming from their finite FOV. Those calculations indicate that only 0.1% of the flux from a source falls in the region between  $128'$  and  $512'$ : we conclude that our aperture corrections are not significantly biased by our use of the  $128'$  models. Later we show that our calibration, when applied to extended sources, gives results consistent with ISO to within 6%. That agreement provides some additional confidence in the accuracy of our aperture corrections.

Application of the model-based aperture corrections to observed PSFs revealed that for apertures  $\leq 48''$  in radius the measured flux depended on aperture size. The reason is the small but systematic difference between the observed and model PSFs at radii of  $\simeq 10''$ – $20''$ , which can be seen in Figure 2. To correct this, we have adopted a hybrid approach to computing the aperture corrections, using the smoothed model PSFs for apertures with radii  $\geq 48''$ , and observed PSFs for smaller apertures. We used observations of 9 asteroids observed using a small  $160\ \mu\text{m}$  map (giving a somewhat larger FOV, as noted earlier), and with fluxes near 1 Jy for the computation. (We also compared these asteroid-based corrections to those based on Pluto (with a color temperature of 55–60 K), and found no measurable difference). The empirical corrections are normalized to the model correction for the  $48''$  aperture. Table 1 lists the resulting hybrid aperture corrections for a selection of photometric aperture sizes, with and without sky annuli, and for a range of source temperatures. Note that these corrections can only accurately be used for sources that are relatively cold (significantly less than 2000 K) – otherwise the near-IR ghost image both alters the PSF, and becomes comparable to or brighter than the  $160\ \mu\text{m}$  image. We have verified that the corrections in Table 1 result in photometry that is independent of aperture size by analyzing 29 cluster-mode asteroid observations, where the targets ranged in brightness from 0.1–4 Jy. The variation with aperture size shows no monotonic trend, and the results for all apertures agree to within 1%.

We performed photometry on our  $160\ \mu\text{m}$  images using an aperture  $24''$  in radius. The small aperture allowed us to increase the SNR of our photometry for the faintest asteroids, and thereby to extend the calibration to somewhat fainter flux densities than would have been possible otherwise. The aperture photometry was corrected to total counts using the aperture correction in Table 1. Photometry at  $24$  and  $70\ \mu\text{m}$  was performed exactly as it was to derive the calibrations in those channels, and as described in Engelbracht et al. (2007) and Gordon et al. (2007). Because a number of our brightest asteroids were in the non-linear response regime at  $70\ \mu\text{m}$  (*i.e.* above a few Jy), we have used PSF-fitting (using the StarFinder package: Diolaiti et al. 2006) to do all of the  $70\ \mu\text{m}$  photometry used here. We

attempted to analyze the 160  $\mu\text{m}$  data using PSF-fitting as well, but the resulting photometry displayed more scatter than did the aperture photometry. We believe this was due to the restricted FOV of the mosaics, and the presence of spatial structure (artifacts) in the images, particularly for fainter sources. An area of concentration in the future will be implementing more robust PSF-fitting algorithms for use at 160  $\mu\text{m}$ .

## 6. Color Corrections

The effective wavelengths of the MIPS channels, defined as the average wavelength weighted by the spectral response function,  $R(\lambda)$ , are  $\lambda_0 = 23.68, 71.42$  and  $155.9 \mu\text{m}$ . The color corrections, which correct the observed in-band flux to a monochromatic flux density at the effective wavelength, are defined by:

$$K = \frac{\frac{1}{F(\lambda_0)} \int F(\lambda) R(\lambda) d\lambda}{\frac{1}{G(\lambda_0)} \int G(\lambda) R(\lambda) d\lambda}.$$

Here  $F(\lambda)$  is the spectrum of the source,  $G(\lambda)$  is the reference spectrum,  $\lambda$  is wavelength,  $F$  and  $G$  are in units of photons/sec/cm<sup>2</sup>/ $\mu\text{m}$ , and  $R$  is in units of  $e^-$ /photon. As defined here, the observed flux should be divided by  $K$  to compute the monochromatic flux density. The MIPS response functions can be obtained from the Spitzer web site (<http://ssc.spitzer.caltech.edu/mips>). For MIPS, the reference spectrum,  $G$ , is chosen as a  $10^4$  K blackbody. While we refer to the 24, 70 and 160  $\mu\text{m}$  channels, we have used the actual effective wavelengths of those channels for all quantitative analyses. For reference, the zero magnitude flux density at 155.9  $\mu\text{m}$  is  $160 \pm 2.45$  mJy. Because the asteroids are much colder (with typical 24:70  $\mu\text{m}$  color temperatures around 250 K), we had to apply color corrections to convert the measured fluxes to monochromatic flux densities at the effective wavelengths. The color corrections for all three MIPS channels and representative source spectra are given in Table 2. In all three channels they are slowly varying functions of temperature above temperatures of 100 K, and also deviate only a few percent from unity at those temperatures. For objects with data at both 24 and 70  $\mu\text{m}$ , the color corrections were computed iteratively based on the 24 and 70  $\mu\text{m}$  flux densities. For the brighter targets lacking 24  $\mu\text{m}$  data, we assumed a temperature of 251 K (see Figure 4), and applied the corresponding color correction.

## 7. Thermal Modeling

The Standard Thermal Model (STM, Lebofsky & Spencer 1989) is the most widely used (therefore “Standard”) model for interpreting observations of thermal emission from

small bodies in the asteroid main belt and the outer Solar System (*c.f.* Campins et al. 1994; Tedesco et al. 2002; Fernández et al. 2002; Stansberry et al. 2006). The model assumes a spherical body whose surface is in instantaneous equilibrium with the insolation, equivalent to assuming either a thermal inertia of zero, a non-rotating body, or a rotating body illuminated and viewed pole-on. In the STM the subsolar point temperature is

$$T_0 = [S_0(1 - p_V q)/(\eta \epsilon \sigma)]^{1/4}, \quad (1)$$

where  $S_0$  is the solar constant at the distance of the body,  $p_V$  is the geometric albedo,  $q$  is the phase integral (assumed here to be 0.39, equivalent to a scattering asymmetry parameter,  $G = 0.15$  (Lumme and Bowell 1981; Bowell et al. 1989)),  $\eta$  is the beaming parameter,  $\epsilon$  is the emissivity (which we set to 0.9), and  $\sigma$  is the Stefan-Boltzmann constant. Given  $T_0$ , the temperature as a function of position on the surface is  $T = T_0 \mu^{1/4}$ , where  $\mu$  is the cosine of the insolation angle. The nightside temperature is taken to be zero. Surface roughness leads to localized variations in surface temperature and non-isotropic thermal emission (beaming). When viewed at small phase angles, rough surfaces appear warmer than smooth ones because the emission is dominated by warmer depressions and sunward-facing slopes. This effect is captured by the beaming parameter,  $\eta$ . Lebofsky et al. (1986) found  $\eta = 0.76$  for Ceres and Vesta; the nominal range for  $\eta$  is 0 to 1, with unity corresponding to a perfectly smooth surface (Lebofsky & Spencer 1989).

The purpose of our thermal modeling is to use the measured 24 and/or 70  $\mu\text{m}$  flux densities to predict the 160  $\mu\text{m}$  flux density for that target. First we correct the flux density from the observed phase angle (typically about 20° for our targets) to 0° using a thermal phase coefficient of 0.01 mag/° (e.g. Lebofsky et al. 1986). We then use the absolute visual magnitude ( $H_V$ , defined for a phase angle of 0°) from Horizons and the relation (e.g. Harris, 1998)  $D = 1329 \times 10^{-H_V/5} p_V^{-1/2}$  to compute the target diameter (where  $D$  is the diameter in km, and  $p_V$  is the visible geometric albedo). Target diameter and albedo are varied until a fit to the observed flux density is achieved. For targets observed at both 24 and 70  $\mu\text{m}$ , the beaming parameter is also varied in order to simultaneously fit both MIPS bands and the visual magnitude. The fitted physical parameters are then fed back into the STM to predict the 160  $\mu\text{m}$  flux density.

Figure 3 illustrates the measured spectral energy distribution (SED) for one of our targets. Also shown are a blackbody and STM fit to the 24 and 70  $\mu\text{m}$  points. The blackbody and STM fits are indistinguishable at the MIPS wavelengths, but small deviations can be seen on the short wavelength side of the emission peak. For the purpose of calibrating the 160  $\mu\text{m}$  channel, we simply require a reliable way to predict the 160  $\mu\text{m}$  flux density by extrapolation from the shorter wavelengths. As the figure demonstrates, the details of the short-wavelength SED do not appreciably affect the predicted 160  $\mu\text{m}$  flux density. Indeed,

we have performed the calibration using both STM and blackbody predictions, and the results are consistent with each other to within better than 1%.

## 8. Results

### 8.1. The 24 $\mu\text{m}$ Subsample

Table 3 summarizes our measurements of targets in the 24  $\mu\text{m}$  sample. Aperture- and color-corrected flux densities are given for the 24 and 70  $\mu\text{m}$  measurements. The 160  $\mu\text{m}$  data are given in the instrumental units, MIPS160, described in § 4.2. As for the shorter wavelengths, the 160  $\mu\text{m}$  measurements have been aperture- and color-corrected. The 24  $\mu\text{m}$  sample makes up one half of the full data set, and covers the faint end of the sample. These observations also allow us to directly determine the color temperatures (used to compute color corrections for individual observations within the sample, and to predict an average color temperature, used to compute color corrections for the 70  $\mu\text{m}$  sample). We also use the 24  $\mu\text{m}$  sample to compute the average 70:160  $\mu\text{m}$  model color for asteroids, which we use to predict 160  $\mu\text{m}$  fluxes for the 70  $\mu\text{m}$  sample.

Figure 4 shows the color temperatures of the objects in the 24  $\mu\text{m}$  sample, determined by fitting a blackbody to the photometry in those channels. The temperatures are fairly tightly clustered, with an average and standard deviation of  $\simeq 251 \pm 25.6$  K. The temperatures are plotted vs. predicted 160  $\mu\text{m}$  flux density. In the context of this figure (only), the prediction is simply the extrapolation of the fitted blackbody curve to 160  $\mu\text{m}$ . Although the range of predicted 160  $\mu\text{m}$  flux densities for the 24  $\mu\text{m}$  sample is only a factor of 5, there is no apparent trend of color temperature. Because the temperatures are fairly similar amongst all the targets, the predicted 160  $\mu\text{m}$  flux density is to first order a measure of the overall apparent thermal brightness of the targets. It then reflects a combination of the influences of distance (heliocentric and Spitzer-centric), albedo, and size. It might be expected that if any of these things were biasing our results, or imposing a systematic trend in the predicted 160  $\mu\text{m}$  flux density (e.g. if our brightest targets were systematically hotter), it would be apparent in this figure.

Given the fairly narrow range of color temperatures we see for the objects in the 24  $\mu\text{m}$  sample, and the insensitivity of the model spectra from 24 to 160  $\mu\text{m}$  to details of the thermal models, we expect the 70  $\mu\text{m}$  to 160  $\mu\text{m}$  color of the asteroids to be quite constant. Figure 5 shows the ratio of the measured 70  $\mu\text{m}$  flux density to the predicted 160  $\mu\text{m}$  flux density for each asteroid in the 24  $\mu\text{m}$  sample. As expected, the color is tightly clustered, with a mean value of 3.77, and a root-mean-square (RMS) scatter of 0.095, or 2.5%. Under the

assumption that asteroids do not possess any strong emissivity variations vs. wavelength in the far-IR, we use this color ratio to interpret our data for the brighter asteroids.

## 8.2. The 70 $\mu\text{m}$ Subsample

Table 4 summarizes our measurements of targets in the 70  $\mu\text{m}$  sample, and is exactly like Table 3 except for the lack of 24  $\mu\text{m}$  data. Making use of the average 70:160  $\mu\text{m}$  color from the 24  $\mu\text{m}$  sample, we compute the predicted 160  $\mu\text{m}$  flux density for the 70  $\mu\text{m}$  sample. The uncertainty on the 160  $\mu\text{m}$  prediction is derived from the uncertainty in the 70  $\mu\text{m}$  measurement root-sum-square (RSS) combined with the 2.5% uncertainty in the average 70:160 color.

## 9. Calibration Factor

Figure 6 shows the calibration factor ( $CF$ ) we derive from our observations of both the 24  $\mu\text{m}$  and 70  $\mu\text{m}$  samples, as a function of the predicted 160  $\mu\text{m}$  flux density. The calibration factor is defined as the predicted flux density at 160  $\mu\text{m}$  divided by the (aperture- and color-corrected) brightness in instrumental units (MIPS160), and by the area of a pixel in steradians.

Of the 102 individual observations, 23 were rejected on the grounds of having 160  $\mu\text{m}$   $\text{SNR} < 4$ ; three more were rejected for having a measured 160  $\mu\text{m}$  flux density more than twice the prediction (these were all for very bright sources, and the discrepancy is due to poorly compensated non-linear response in the 70  $\mu\text{m}$  channel resulting in predictions that were too low. Figure 6 shows the remaining 76 values of the calibration factor. There is a fairly clear trend of increasing calibration factor for predicted flux densities greater than about 2 Jy. We attribute this trend to a non-linear response of the detectors for bright targets. This effect is similar in magnitude to that seen at 70  $\mu\text{m}$ , also at flux densities greater than about 1–2 Jy (Gordon et al. 2007). For the moment we exclude the 19 points above 2 Jy from consideration. Taking the points below 2 Jy, we compute the average and RMS scatter, and identify as outliers 8 points that deviate from the mean by more than 1.5 times that scatter (indicated by circled points in Figure 6). We use the weighted mean of the remaining 49 values to compute the calibration factor for the MIPS 160  $\mu\text{m}$  channel. Use of the weighted mean ensures that a source with zero flux produces zero response if all of the inputs to the calibration (e.g. dark current, linearity) are perfectly known.

The weighted mean calibration factor is  $CF = 41.7 \text{ MJy/sr/MIPS160}$ , and the RMS

scatter is 4.82 MJy/sr/MIPS160. This suggests an uncertainty of 11.6% for the determination of the flux density of a particular source based on a single measurement. The formal uncertainty on the average calibration factor is 0.69 MJy/sr/MIPS160, or only 1.6%, but this value clearly underestimates the uncertainty that should be assumed when interpreting 160  $\mu\text{m}$  photometry (see below). The average calibration factor and RMS scatter are shown in Figure 6 as the horizontal dashed lines. Below we discuss other sources of uncertainty in the calibration. The final value and uncertainty we adopt are  $41.7 \pm 5.0$  MJy/sr/MIPS160 (equivalent to a 12% uncertainty). This calibration is valid for sources with 155.9  $\mu\text{m}$  flux densities  $\leq 2$  Jy.

We also computed a weighted linear fit to the data, but in this case include those points with predicted 160  $\mu\text{m}$  flux densities  $> 2$  Jy. Based on the linear fit,  $CF = (39.24 + 2.58 \times P_{160})$  MJy/sr/MIPS160, where  $P_{160}$  is the predicted 160  $\mu\text{m}$  flux density. The formal uncertainties on the intercept and slope from the linear fit are 1.29 MJy/sr/MIPS160 and 0.76 MJy/sr/MIPS160/Jy, respectively, indicating that the slope is significant at the  $3.4\sigma$  level. This reflects the influence of the response non-linearity above 2 Jy, and can be used to provide an approximate calibration of targets with flux densities  $> 2$  Jy. Inspection of the points in Figure 6 suggest that the non-linearity may affect photometry at the 20% level for targets with flux densities near 4 Jy, somewhat more than would be derived based on the linear fit to the data.

### 9.1. Uncertainty on the 160 $\mu\text{m}$ Absolute Calibration

As suggested above, observers are typically more interested in the uncertainty they should assume for the flux density they determine from a single observation of a target than they are in the formal uncertainty on the calibration factor determined from an ensemble. Here we compare the 11.6% uncertainty estimated above to the uncertainty we would expect given the other uncertainties in the inputs to the calibration. The relevant uncertainties to consider are: 1) the photometric repeatability at 160  $\mu\text{m}$ , 2) the uncertainties in the 24  $\mu\text{m}$  and 70  $\mu\text{m}$  calibrations, 3) systematic uncertainties associated with color and aperture corrections, and 4) uncertainties inherent to the models used in the calibration.

We have assessed the photometric repeatability of the 160  $\mu\text{m}$  channel two ways. Because we have relatively few repeated observations of stable (i.e. non-asteroidal), red sources, we analyzed 81 160  $\mu\text{m}$  observations of a stellar calibrator (HD 163588), and found that those measurements exhibited an RMS scatter of 3.4%. While those data are severely impacted by the short-wavelength ghost, they do provide a valid measure of the repeatability delivered by the readout electronics and the end-to-end data analysis for a very bright source. We

have also analyzed 5  $160\ \mu\text{m}$  observations of IRAS 03538-6432, which has a very red near-IR: $160\ \mu\text{m}$  color, and a  $160\ \mu\text{m}$  flux density of  $\simeq 1.04$  Jy (Klass et al. 2001), finding an RMS scatter of 5.5%. We adopt 5% as our current estimate of the repeatability.

The uncertainties in the calibrations of the shorter MIPS bands are estimated to be 2% ( $24\ \mu\text{m}$ : Engelbracht et al. 2007) and 5% ( $70\ \mu\text{m}$ : Gordon et al. 2007). As noted earlier, taken in combination and ignoring any other uncertainties, these place a lower limit on the  $160\ \mu\text{m}$  calibration uncertainty of 7%. The color corrections we have applied are very modest (a few percent), and so are unlikely to contribute significantly to the calibration uncertainty. The 24 and  $70\ \mu\text{m}$  photometry was done identically to the way it was done for the calibrations of those bands, and so should not impose any additional uncertainty or systematic bias on the results used here.

The  $160\ \mu\text{m}$  aperture correction we used, 2.60, is large and is probably uncertain at the level of a few percent. Uncertainty in the aperture correction will be irrelevant if others use the same aperture (*i.e.*  $24''$ , with a sky annulus of  $64''$ – $128''$ ) and correction to perform photometry of point sources, and we encourage observers to use this aperture when practical. However, we can not assume that such will be the case. Checks of  $160\ \mu\text{m}$  measurements of extended sources (see below) against previous missions suggest agreement to within about 6%, suggesting that our aperture corrections are reasonably accurate. As noted earlier, we find no evidence to suggest that the aperture correction for the  $24''$  aperture is any more uncertain than that for a  $48''$  aperture, where the aperture correction is a more modest (and model-based) 1.60. For lack of good  $160\ \mu\text{m}$  observations to further assess the uncertainty in the aperture corrections, and based on our experience with the 24 and  $70\ \mu\text{m}$  calibrations, we adopt an uncertainty of 3% for our  $160\ \mu\text{m}$  aperture corrections. This uncertainty should be interpreted as applying to the  $48''$  aperture, and as being empirically verified as transferable to the  $24''$  aperture.

The final uncertainty in the calibration is associated with the assumptions inherent in the Standard Thermal Model, particularly the spectral emissivity in the  $24\ \mu\text{m}$ – $160\ \mu\text{m}$  range. As noted earlier, we have assumed a gray emissivity, whereas there are suggestions from ISO observations that the emissivity of some asteroids may decline by 10% or so in this region (e.g. Müller and Lagerros, 2002). We find that our 24 and  $70\ \mu\text{m}$  measurements of asteroids, when fit independently with the STM, give diameters for the targets that agree to within 3%, with an RMS scatter of 5% (the  $70\ \mu\text{m}$  diameters being smaller). This suggests that there is no strong decrease of emissivity for the asteroids in our sample between 24 and  $70\ \mu\text{m}$  (because those calibrations are derived solely from observations of stars). Unfortunately we can not make a similar argument about emissivity in the range  $70$ – $160\ \mu\text{m}$  based on our data. We adopt an uncertainty of 5% to account for our lack of knowledge of the spectral

emissivity at  $160\ \mu\text{m}$ , and as being consistent with the lack of evidence for any measurable emissivity trend from  $24\text{--}70\ \mu\text{m}$ .

If we RSS combine the uncertainties just discussed, we predict that the  $160\ \mu\text{m}$  calibration should be accurate to 10.4%, which is very consistent with the 11.6% uncertainty estimated from the RMS scatter of the calibration factor values in Figure 6. While the combined effect of the calibration uncertainties at  $24$  and  $70\ \mu\text{m}$  are the largest single contributor to the  $160\ \mu\text{m}$  uncertainty, the other uncertainties together are at least as important. Given that emissivity effects would result in a systematic bias in our calibration, we should not really RSS it with the other uncertainties. If we RSS-combine the other uncertainties, and then simply add the 5% uncertainty for emissivity effects, we predict a worst-case uncertainty of 14.1% in the calibration (worst-case because it assumes that the net effect of the random uncertainties combine constructively with the emissivity uncertainty). Given the general agreement in the magnitude of these estimates and that based on the RMS scatter of the measurements of  $CF$  itself, we adopt an uncertainty of 12% for the absolute calibration of the  $160\ \mu\text{m}$  channel of MIPS.

## 9.2. Calibration Cross Checks

Soon after the launch of *Spitzer*, observations of a few targets that have well-studied SEDs in the  $160\ \mu\text{m}$  region were made, and formed the basis of the initial calibration. These included observations of a few asteroids (those data were included in the analysis above), which led to  $CF = 41.6 \pm 8.5$  MJy/sr/MIPS160. Observations of K-giant calibration stars were affected by the near-IR ghost, but after roughly correcting for the ghost, those data indicated  $CF = 37.8 \pm 11.3$  MJy/sr/MIPS160. Early science observations of Fomalhaut were also analyzed, and indicated  $CF = 39.8 \pm 6.0$  MJy/sr/MIPS160. We also analyzed early science data for M33 (Hinz et al., 2004), NGC 55, NGC 2346, and the Marano Strip, which, taken together, indicated  $CF = 46.8 \pm 12$  MJy/sr/MIPS160. All of these results lead us to adopt an initial calibration for the  $160\ \mu\text{m}$  channel of  $CF = 42.5 \pm 8.5$  MJy/sr/MIPS160. Gordon et al. (2006) have compared MIPS  $160\ \mu\text{m}$  measurements of M31 to DIRBE and ISO measurements, finding excellent agreement. All of these provide a sanity check of the new calibration, because it is only 1.9% lower than the initial calibration.

More recently we have compared MIPS measurements of a few ULIRGs to ISO measurements of the same objects, and to the IRAS results for the asteroids observed for the MIPS  $160\ \mu\text{m}$  calibration program. In both of these cases we have included comparisons at the shorter MIPS bands as well as at  $160\ \mu\text{m}$ . The comparisons at the shorter wavelengths serve two purposes. Because both the  $24$  and  $70\ \mu\text{m}$  calibrations are entirely based on ob-



servations of stars, any short-wavelength spectral leaks present in those channels would bias photometry of cold sources such as ULIRGs and asteroids: the comparisons serve to confirm the lack of such leaks. Because the  $160\ \mu\text{m}$  calibration is derived directly from the shorter MIPS bands, the comparisons at those wavelengths also serve to confirm the validity of the  $160\ \mu\text{m}$  calibration, even though it (unlike for the shorter bands) is based on observations of red sources.

We reduced Spitzer archive data for the ULIRGs IRAS 03538-6432 (5 epochs), IRAS 13536+1836, IRAS 19254-7245 and IRAS 20046-0623 (1 epoch for each), and measured their flux densities at 70 and  $160\ \mu\text{m}$ . The  $70\ \mu\text{m}$  flux densities for the first three was within a few percent of the values we would expect based on the ISO photometry reported by Klaas et al. (2001). In particular, for the first two, the MIPS and ISO results agreed to better than a percent. The  $160\ \mu\text{m}$  flux densities were 5% higher than expected from the ISO data on average. Again, for IRAS 03538-6432 the agreement was within 1%. The MIPS data for IRAS 20046-0623 gave 70 and  $160\ \mu\text{m}$  flux densities 25%–30% lower than would be expected from the ISO data, but there is no obvious reason for this discrepancy (e.g. no bright background objects that might have fallen within the ISO beam).

We have also fitted our 24 and  $70\ \mu\text{m}$  observations of asteroids with the STM, deriving diameters for all our targets. The diameters we derive by fitting the two bands independently (for the faint sample) agree quite well: the mean and RMS scatter of the ratio of the diameters determined at  $24\ \mu\text{m}$  to those determined at  $70\ \mu\text{m}$  being 1.02 and 0.051, respectively. This confirms that the calibrations of these two bands are very consistent when applied to observations of red sources. The small deviation of this ratio from unity has a formal significance of  $2.8\sigma$ , but could easily be due to the failure of the simple assumptions of the STM to fully describe the thermal emission. We also have compared the diameters determined from our data to the diameters derived from IRAS data (the SIMPS catalog, Tedesco et al. 2002). The average and RMS scatter of the ratios of the MIPS diameters to the IRAS diameters at  $24\ \mu\text{m}$  are 1.01 and 0.09, while at  $70\ \mu\text{m}$  they are 0.99 and 0.10. We conclude that our calibration in those bands is entirely consistent with the IRAS calibration; by inference the  $160\ \mu\text{m}$  calibration should also be consistent with IRAS.

### 9.3. Extended Source Calibration

We also checked the calibration on extended sources at  $160\ \mu\text{m}$ , using observations of a handful of resolved galaxies which were observed by ISOPHOT using the C\_160 broad band filter ( $\lambda_{ref} = 170\ \mu\text{m}$ ). The galaxies used for this comparison are M31 (Haas et al. 1998; Gordon et al. 2006), M33 (Hippelein et al. 2003; Hinz et al. 2004), M101 (Stickel et al.

2004; Gordon et al. 2006, in prep.), and NGC3198, NGC3938, NGC6946, and NGC7793 (Stickel et al. 2004; Dale et al. 2005, 2007). These objects range in diameter from 5–10' (the NGC objects) to  $\geq 0.5^\circ$  (the Messier objects), and so are all highly resolved by both MIPS at  $160\ \mu\text{m}$  (40" FWHM) and ISOPHOT at  $170\ \mu\text{m}$  (90" pixels). We applied color corrections to the MIPS and ISOPHOT measurements, and corrected for the difference in wavelengths, assuming the emission has a color temperature of 18 K. The resulting average ratio and uncertainty in the mean of the MIPS  $160\ \mu\text{m}$  to ISOPHOT  $170\ \mu\text{m}$  flux densities is  $0.94 \pm 0.06$ . If the emissivity of the dust in these galaxies is proportional to  $\lambda^{-2}$ , the expected ratio of the measurements is 1.00, consistent to within the uncertainty in the measured mean. Thus the MIPS and ISOPHOT extended-source calibrations near  $160\ \mu\text{m}$  are entirely consistent with one another. These comparisons also indicate that the MIPS point-source derived calibration at  $160\ \mu\text{m}$  is directly applicable to observations of extended sources, and by inference that the aperture corrections in Table 1 are accurate to within a few percent.

#### 9.4. $160\ \mu\text{m}$ Enhanced AOT: Calibration and Sensitivity

In Spring of 2007 a new  $160\ \mu\text{m}$  photometry observing template (the “Enhanced AOT” was made available. The goal of the new template is to allow  $160\ \mu\text{m}$  photometry data to be time filtered, as has been done all along for the  $70\ \mu\text{m}$  data. A limited number of observations (3) taken using the enhanced  $160\ \mu\text{m}$  AOT were available at the time of this writing. In each case, the same target was observed using the standard  $160\ \mu\text{m}$  AOT as well.

All of these data were reduced in the standard manner, as described earlier. In addition, the enhanced AOT data were processed by applying a high-pass time-domain filter to the time series for each pixel (this filtering process is a standard part of the reduction at  $70\ \mu\text{m}$ : Gordon et al. 2005; 2007). Because a dither is performed between all images, the filter preserves the signal from point sources while suppressing elevated noise levels that result from signal drifts in un-filtered data products. Such filtering can not reliably be applied to data from the standard AOT because the dithers never completely move the source out of the FOV of the array. The result is that time-filtering erodes flux from the target source, and does so in a way that is flux dependent. The enhanced AOT implements a wider dither pattern, providing enough data away from the source that the filter works well.

Photometry on the standard AOT, enhanced AOT without time-filtering, and enhanced AOT with time-filtering was measured as described earlier. We draw preliminary but encouraging conclusions based on these initial results. 1) Photometry measured on the standard and enhanced AOT data agree to within about 5%, except on bright ( $> 1\ \text{Jy}$ ) sources, where

the time-filtered product gives systematically lower fluxes (at about the 10% level). Thus, the enhanced AOT should only be utilized for sources expected to be fainter than about 1 Jy. 2) The time-filtered enhanced AOT data provides significant sensitivity improvements over the standard AOT, unfiltered data. We computed the  $1\sigma$ , 500 second noise-equivalent flux density (NEFD, frequently referred to as “sensitivity”). For the old AOT NEFD= 35 mJy, while for the enhanced AOT NEFD= 22 mJy. Thus the enhanced AOT improves the point-source sensitivity of the  $160\ \mu\text{m}$  channel by about 35%. We lacked sufficient data to compare the repeatability of the enhanced AOT relative to the old AOT, but expect that it may result in some significant gains, particularly for faint sources and/or higher backgrounds.

## 10. Summary

We have undertaken a program to calibrate the MIPS  $160\ \mu\text{m}$  channel using observations of asteroids. The strategy employed was statistical in nature: rather than perform detailed modeling of a few asteroids to try and accurately predict their  $160\ \mu\text{m}$  flux density for our observing circumstances, we instead rely on the average emission properties of asteroids in the spectral range  $24 - 160\ \mu\text{m}$  to allow us to transfer the calibration of our 24 and  $70\ \mu\text{m}$  channels to the  $160\ \mu\text{m}$  channel. Our 24 and  $70\ \mu\text{m}$  data from 51 observations (1/2 of the total, the other 51 did not include  $24\ \mu\text{m}$  data) indicate that asteroid spectral energy distributions are indeed all quite similar at these long wavelengths, providing *post facto* support for the strategy. The calibration factor we derive, which converts the instrumental units of the  $160\ \mu\text{m}$  channel (MIPS160) to surface brightness, is  $41.7\ \text{MJy/sr/MIPS160}$ , with a formal uncertainty (uncertainty of the mean) of  $0.69\ \text{MJy/sr/MIPS160}$ . Including the effects of the uncertainties in the 24 and  $70\ \mu\text{m}$  calibrations, the observed repeatability of  $160\ \mu\text{m}$  measurements of a stellar calibrator and a ULIRG, and allowing for expected uncertainties in aperture and color corrections, and modeling uncertainties, we adopt an uncertainty of 12% on the  $160\ \mu\text{m}$  flux determined from an individual measurement of a source. Cross-checks of this calibration against those of ISO measurements of ULIRGS and nearby galaxies, and against IRAS measurements of asteroids, show that the MIPS calibration is quite consistent with those earlier missions.

This work is based on observations made with the *Spitzer Space Telescope*, which is operated by the Jet Propulsion Laboratory, California Institute of Technology under NASA contract 1407. Support for this work was provided by NASA through Contract Number #1255094 issued by JPL/Caltech. Ephemerides were computed using the services provided by the Solar System Dynamics group at JPL. We thank an anonymous reviewer for inputs which improved this paper significantly. And, we acknowledge the wise insight of Douglas

Adams, who pointed out over 20 years ago that the answer *is* 42.

## REFERENCES

- Beichmann, C.A. et al. 1985. Infrared Astronomical Satellite (IRAS) Catalogs and Atlases Explanatory Supplement”, ed. C. A. Beichman, G. Neugebauer, H. J. Habing, P. E. Clegg, and T. J. Chester. U. S. Government Printing Office.
- Bowell, E. et al. 1989, in Asteroids II, ed. R. P. Binzel, T. Gehrels, T., & M. S. Matthews (Tucson: Univ. Arizona Press)
- Campins, H. et al. 1994, AJ 108, 2318
- Dale, D.A. et al. 2005, ApJ 633, 857
- Dole, H., et al. 2006, A&A 451, 417
- Dale, D.A. et al. 2007, ApJ 655, 863
- Diolaiti, E. et al. 2000, A&AS 147, 335
- Engelbracht, C.W. et al. 2007, this issue
- Fazio, G. et al. 2004 ApJS 154, 10
- Fernandez, Y.F. et al. 2002, AJ 123, 2050
- Fixsen, D.J. et al. 1997, ApJ 490, 482
- Gordon, K.D., et al. 2007, in prep.
- Gordon, K.D., et al. 2007, this issue.
- Gordon, K.D. et al. 2005, PASP 117, 503
- Gordon, K.D., et al. 2006, ApJ 638, 87
- Haas, M. et al, 1998, A&A 338, L33
- Harris, A.W. 1998. Icarus 131, 291
- Hauser, M.G. et al., 1998 ApJ 508, 25-43)
- Hinz, J.L. et al 2004, ApJS, 154, 259
- Hippelein, H. et al., 2003, A&A 315, L82
- Hora, J.L. et al. 2004, SPIE 5487, 77

- Houck, J.R. et al. 2004, ApJS 154, 18
- Klaas, U. et al. 2001, A&A 379, 823
- Krist, J. 2002, Tiny Time/SIRTF User's Guide (Pasadena: SSC)
- Lebofsky, L. A, et al. 1986, Icarus 68, 239.
- Lebofsky, L. A, & Spencer, J. R. 1989, in Asteroids II, ed. R. P.Binzel, T. Gehrels, T., & M. S. Matthews (Tucson: Univ. Arizona Press)
- Lebofsky, L.A. et al. 1986, Icarus 68, 1694
- Lumme, K. and E. Bowell 1981, AJ 86, 1694
- Mather, J.C. et al. 1999, ApJ 512, 511
- Müller, T.G, and J.S.V. Lagerros, 1998, A&A 338, 340
- Müller, T.G, and J.S.V. Lagerros, 2002, A&A 381, 324
- Neugebauer, G. et al. 1984, ApJ 278, 1
- Reach, W.T. et al. 2005, PASP 117, 978
- Rieke, G.H. et al. 2004, ApJS 154, 25
- Rieke, G.H. et al. 2007, in prep.
- Schulz, B. et al. 2002, A&A 381, 1110
- Stansberry, J.A. et al. 2006, ApJ 643, 556
- Stickel, M. et al. 2004, A&A 422, 39
- Tedesco, E. F. et al. 2002, AJ 123, 2056
- Werner, M.W. et al. 2004, ApJS 154, 1

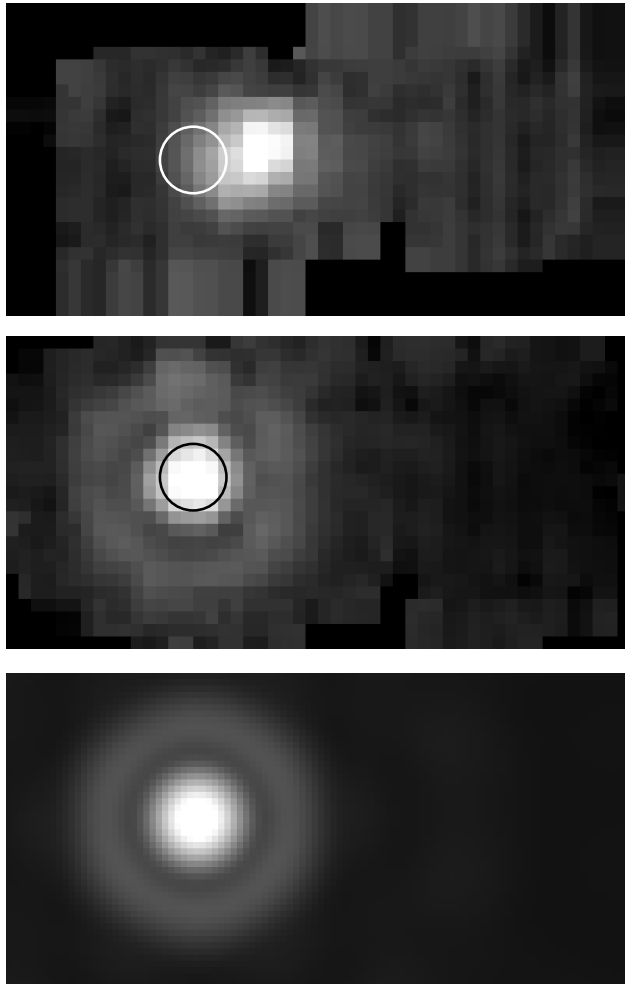


Fig. 1.— MIPS  $160\ \mu\text{m}$  images of a star (HD 163588, top), an asteroid (471 Papagena, middle), and an STinyTim-based model PSF (bottom). The star image is dominated by the near-IR ghost image (see text), while the asteroid image reveals no measurable contamination from the ghost image. For typical asteroids, the ghost image will be  $\gtrsim 2000$  times fainter, relative to the  $160\ \mu\text{m}$  image, than for stars. The circles are centered at the pointing used in each observation. The ghost image is always offset from the nominal pointing towards the array centerline. The slightly different FOV of the two images (note missing data and replicated pixels around the edge of the mosaic of the star) results from the use of a small (3-point) map for the asteroid observation. The mosaics were generated using a pixel scale of  $8''$ ,  $\simeq 1/2$  the native pixel scale of the  $160\ \mu\text{m}$  array. The model PSF was generated using STinyTim (see text) with a pixel scale of  $3.2''$  and then smoothed using a boxcar 8 pixels ( $25.6''$ ) in width, equivalent to 1.6 native pixels. Each image is  $6.5'$  across; the circles in the upper panels are  $40''$  across.

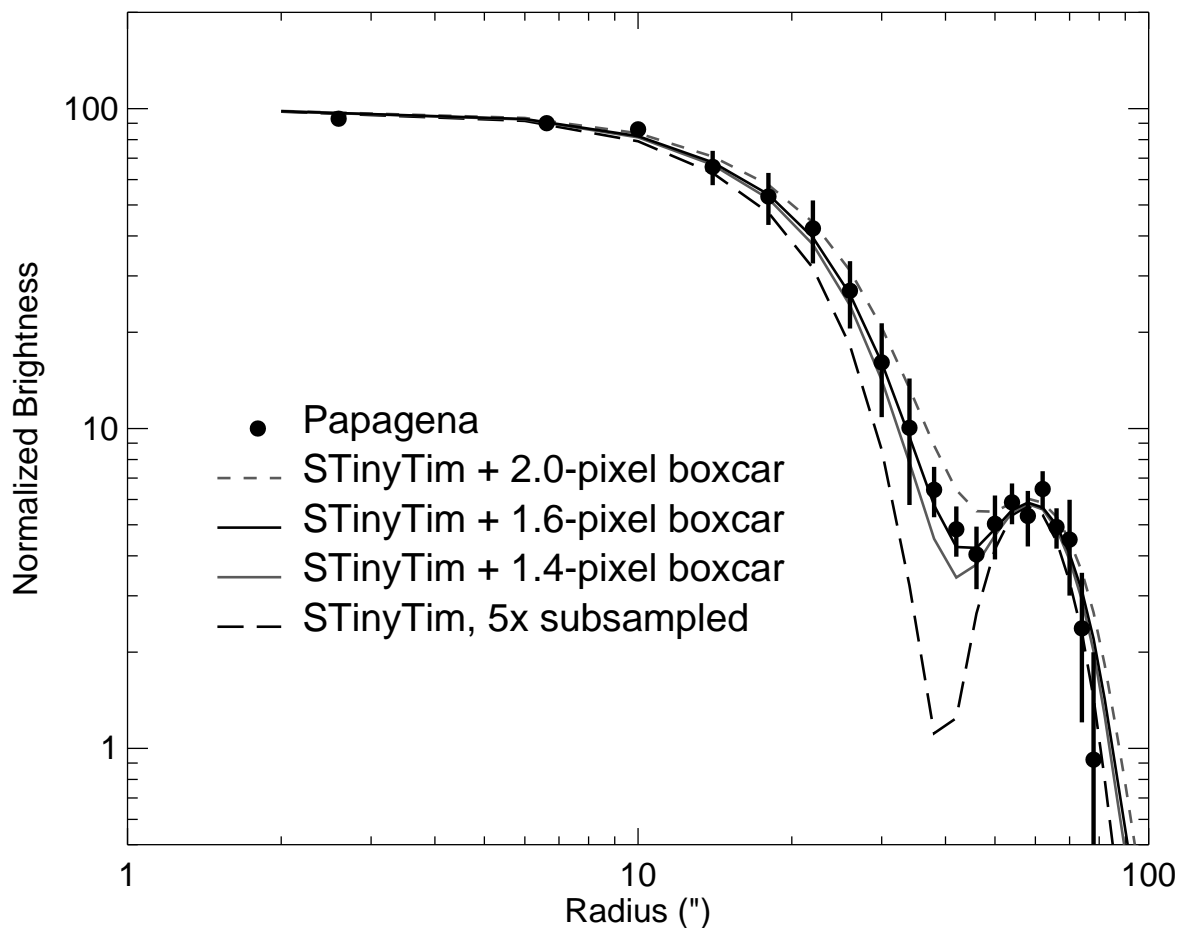


Fig. 2.— An observed  $160\ \mu\text{m}$  PSF radial profile is compared to 4 STinyTim model PSF radial profiles. The observed profile (filled circles) is derived from the observation of asteroid 471 Papagena shown in Figure 1; error bars indicate the scatter within each radial bin. The mosaic used to generate the profile has pixels  $8''$  square. The model PSFs were generated with  $3.2''$  square pixels (5x oversampled). Various smoothings were then applied to the model PSF to match the shape of the observed PSF. Smoothing with a boxcar equivalent to 1.6 native pixels ( $25.6''$ ) results in an excellent match with the observed PSF. The FWHM of the observed PSF is  $38.3''$ , and for the model it is  $38''.2$ .



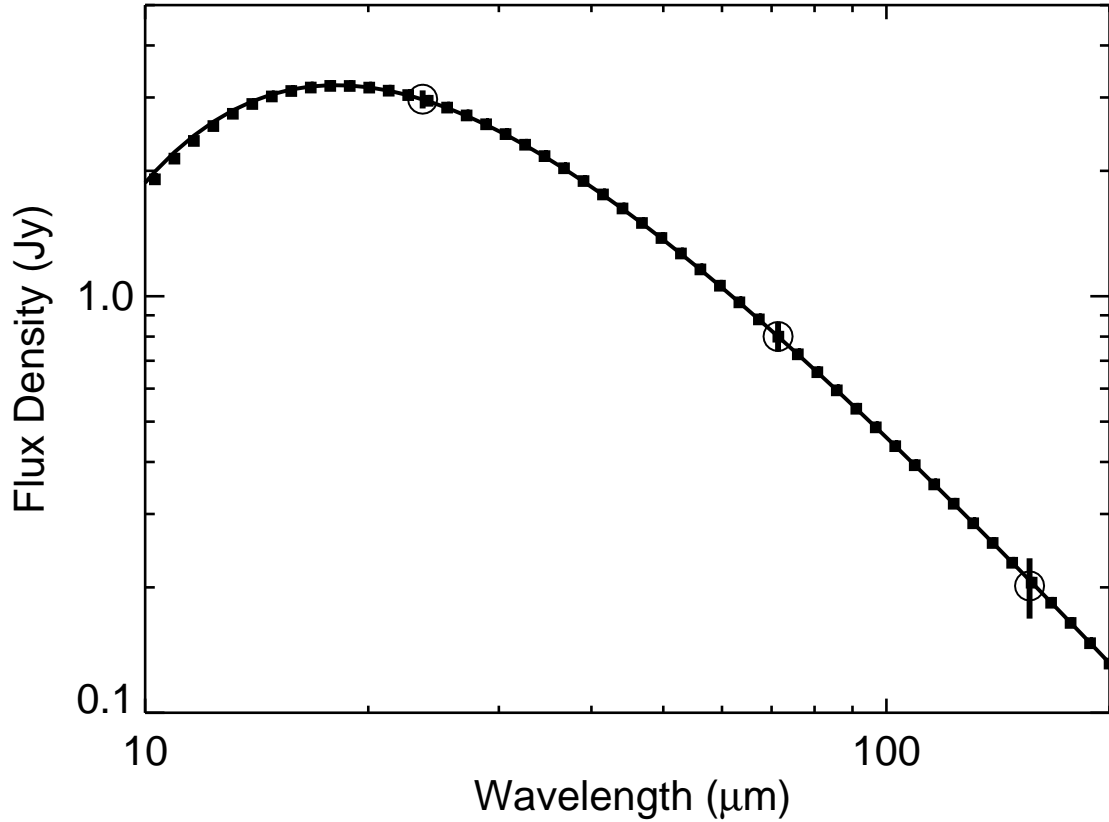


Fig. 3.— The spectral energy distribution for asteroid 282 Clorinde is compared to blackbody and standard thermal model (STM) fits. The measured SED in the MIPS channels is shown as filled circles with error bars (the error bars are the root-sum-square of the measurement uncertainty determined from the images and the calibration uncertainties in each channel). The small square symbols trace a blackbody fit to the data; the solid line shows the STM fit. The 160  $\mu\text{m}$  point is plotted using the calibration derived here, but was not used in the fits.

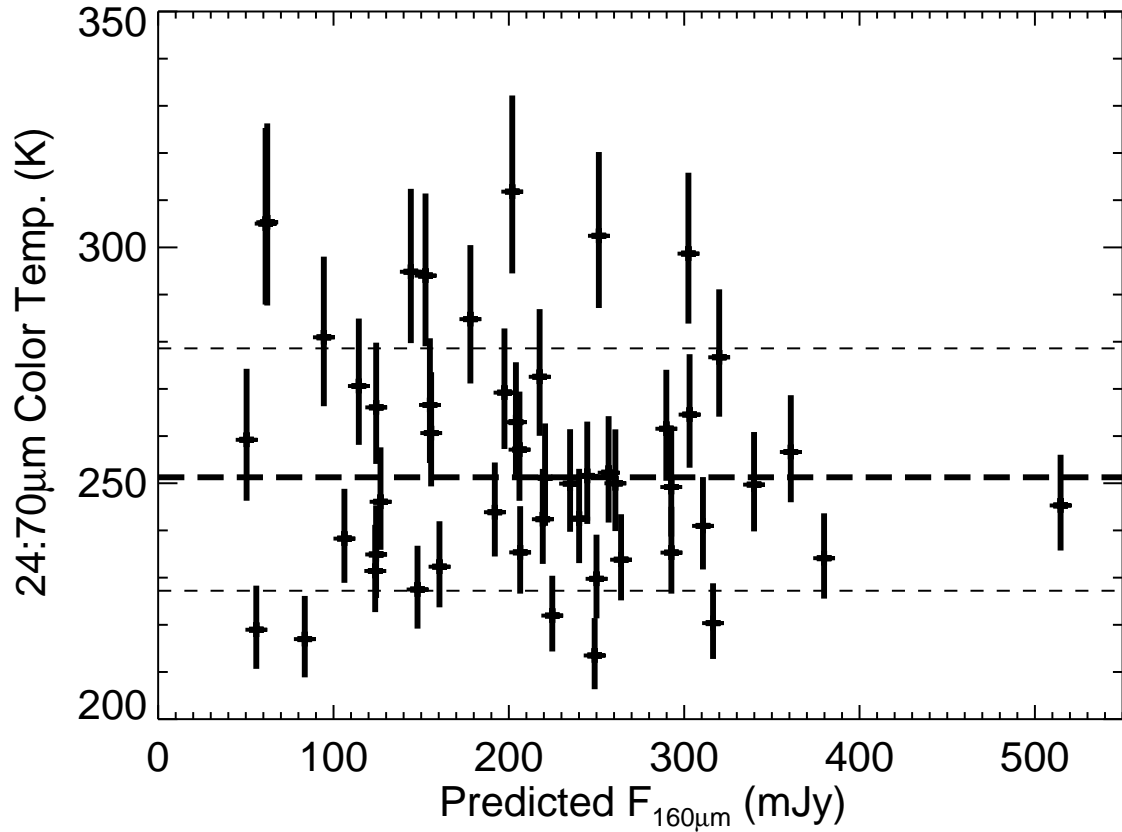


Fig. 4.— The color temperature of those asteroids faint enough to be observed at  $24\ \mu\text{m}$ . The color temperature is computed by fitting the  $24$  and  $70\ \mu\text{m}$  photometry with a blackbody. Error bars are computed by fitting a blackbody to the flux densities  $\pm 1\sigma$ . The average  $24:70$  color temperature is  $251\ \text{K}$ , and the standard deviation is  $26\ \text{K}$  (shown by the thin dashed lines).

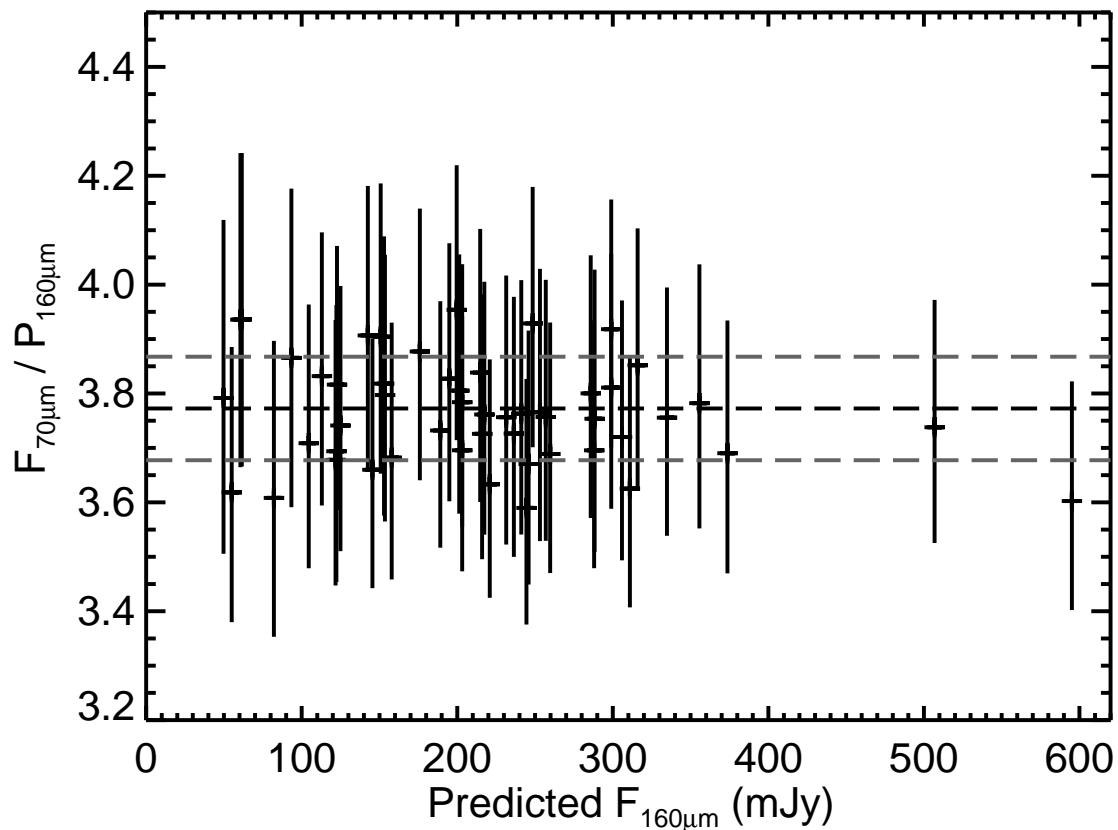


Fig. 5.— The ratio of the measured  $70\ \mu\text{m}$  flux density to the  $160\ \mu\text{m}$  flux density predicted from STM fits to the  $24$  and  $70\ \mu\text{m}$  photometry for objects in the  $24\ \mu\text{m}$  (faint) sample. The average  $70:160\ \mu\text{m}$  model color (dashed line) is  $3.77 \pm 0.095$ , where the uncertainty is computed as the RMS scatter of the individual predictions. The formal error on the average color is  $0.014$ , or about  $0.4\%$ .

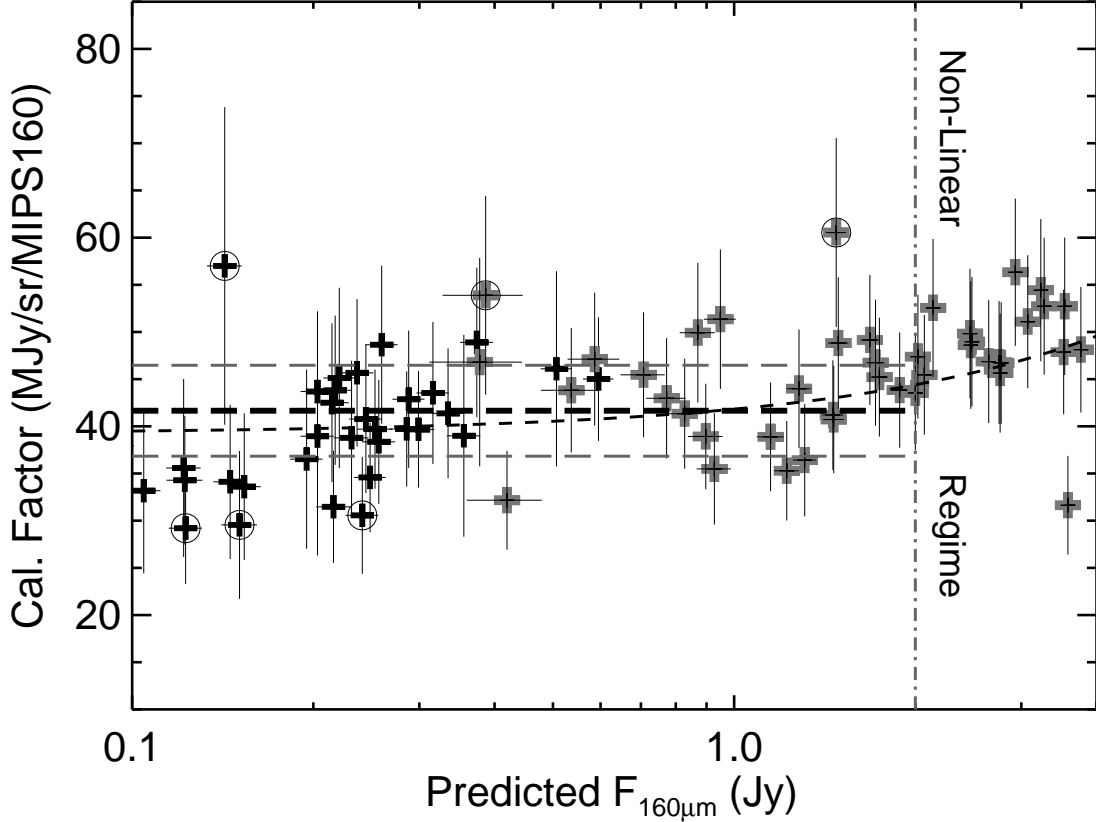


Fig. 6.— The calibration factor for the MIPS 160  $\mu\text{m}$  channel vs. the predicted 160  $\mu\text{m}$  flux density of the asteroids we observed. Black plus symbols represent the objects in the 24  $\mu\text{m}$  (faint) sample, which were observed at 24, 70, and 160  $\mu\text{m}$ . Grey plus symbols represent objects in the 70  $\mu\text{m}$  (bright) sample, which was observed at 70 and 160  $\mu\text{m}$ . One- $\sigma$  uncertainties are indicated by thin error bars. Data points that are circled were excluded from our calculation of the calibration factor because they are discrepant at or above  $1.5\sigma$ . Above about 2 Jy the response of the detectors becomes non-linear, so the points above that are also excluded: formally, the calibration only applies below 2 Jy. The heavy long-dashed line shows the weighted-average calibration factor,  $CF = 41.7 \pm 0.69$  MJy/sr/MIPS160. The RMS scatter of the data is 4.82 MJy/sr/MIPS160, as shown by the thin, gray, long-dashed lines. The short-dashed line shows a linear fit to the data (including points  $> 2$  Jy), which yields  $CF = 39.2 \pm 1.80$  MJy/sr/MIPS160, with a slope of  $2.58 \pm 0.76$  MJy/sr/MIPS160/Jy. This calibration curve can be used to approximately calibrate targets with measured flux densities  $> 2$  Jy.

Table 1. MIPS 160  $\mu\text{m}$  Aperture Corrections

Temp.(K)	Aperture Radius					
	16''	24''	32''	40''	48''	64''
No Sky Annulus						
10	4.761	2.657	2.011	1.776	1.634	1.402
30	4.677	2.610	1.976	1.745	1.605	1.355
50	4.665	2.603	1.971	1.740	1.601	1.348
150	4.651	2.595	1.965	1.735	1.596	1.341
250	4.648	2.593	1.963	1.734	1.595	1.340
500	4.648	2.593	1.963	1.734	1.595	1.339
2000 <sup>b</sup>	4.645	2.592	1.962	1.733	1.594	1.339
With Sky Annulus <sup>a</sup>						
10	4.785	2.670	2.021	1.785	1.642	1.406
30	4.697	2.621	1.984	1.752	1.612	1.361
50	4.683	2.613	1.978	1.747	1.607	1.354
150	4.668	2.605	1.972	1.741	1.602	1.348
250	4.665	2.603	1.971	1.740	1.601	1.347
500	4.662	2.602	1.970	1.739	1.600	1.346
2000 <sup>b</sup>	4.662	2.602	1.970	1.739	1.600	1.345

<sup>a</sup>The sky annulus radius was 64''–128'' for apertures up to 48'', and was 80''–160'' for the 64'' aperture.

<sup>b</sup>Note that sources with near-IR:160  $\mu\text{m}$  color temperatures  $\geq 2000$  K are subject to additional, large photometric uncertainty due to the contribution from the near-IR ghost image.

Table 2. MIPS Color Corrections<sup>a</sup>

	$\lambda_0(\mu m)$		
	23.68	71.42	155.9
Blackbody Spectrum			
T(K)			
10000.0	1.000	1.000	1.000
1000.0	0.992	0.995	0.999
300.0	0.970	0.980	0.996
150.0	0.948	0.959	0.991
100.0	0.947	0.938	0.986
80.0	0.964	0.923	0.982
70.0	0.986	0.914	0.979
60.0	1.029	0.903	0.976
50.0	1.119	0.893	0.971
40.0	1.335	0.886	0.964
35.0	1.569	0.888	0.959
30.0	2.031	0.901	0.954
25.0	3.144	0.941	0.948
20.0	7.005	1.052	0.944
Power Law ( $\nu^\beta$ )			
$\beta$			
-3.0	0.967	0.933	0.965
-2.0	0.960	0.918	0.959
-1.0	0.961	0.918	0.959
0.0	0.967	0.932	0.965
1.0	0.981	0.959	0.979
2.0	1.001	1.001	1.000
3.0	1.027	1.057	1.029

<sup>a</sup>Divide measured fluxes by these values to compute the corrected monochromatic flux density.

Table 3. 24  $\mu\text{m}$  (Faint) Sample

#	Asteroid	Obs. Date	AORKEYS <sup>a</sup>								MIPS160 <sup>c</sup>	<i>err</i> <sub>M160</sub> <sup>c</sup>	CF <sup>d</sup>
			24+70	160	<i>F</i> <sub>24</sub> <sup>b</sup>	<i>err</i> <sub>24</sub> <sup>b</sup>	<i>F</i> <sub>70</sub> <sup>b</sup>	<i>err</i> <sub>70</sub> <sup>b</sup>	<i>P</i> <sub>160</sub> <sup>b</sup>	<i>err</i> <sub>P160</sub> <sup>b</sup>			
186	Celuta	2004-02-23		9064960	4.612	0.231	1.345	0.139	0.356	0.049	1.516	0.406	38.99
248	Lameia	2004-02-23		9065216	3.585	0.179	1.082	0.115	0.288	0.041	1.516	0.491	31.60
443	Photographica	2004-02-23		9065728	2.089	0.104	0.584	0.063	0.153	0.022	0.628	0.390	40.46
186	Celuta	2004-03-18		9193216	2.700	0.135	0.902	0.093	0.246	0.034	1.053	0.377	38.82
25	Phocaea	2004-03-18		9193728	3.618	0.181	1.138	0.117	0.306	0.042	1.961	0.869	25.93
432	Pythia	2004-03-18		9193984	3.186	0.159	1.127	0.116	0.311	0.042	0.827	0.372	62.50
284	Amalia	2004-04-07		9460224	3.805	0.190	1.086	0.112	0.286	0.039	1.196	0.249	39.72
783	Nora	2004-04-07		9460736	6.159	0.308	1.895	0.195	0.507	0.069	1.827	0.445	46.09
432	Pythia	2004-04-07		9460992	2.329	0.116	0.589	0.062	0.151	0.021	0.848	0.224	29.55
1584	Fuji	2004-04-08		9460480	1.574	0.079	0.433	0.046	0.113	0.016	0.718	0.223	26.16
1584	Fuji	2004-05-02		9664512	0.993	0.050	0.242	0.027	0.061	0.009	0.577	0.159	17.71
60	Echo	2004-05-07		9665792	2.890	0.145	0.869	0.091	0.231	0.032	0.992	0.234	38.78
1137	Raissa	2004-05-07		9666048	0.654	0.033	0.189	0.022	0.050	0.008	0.328	0.114	25.22
1584	Fuji	2004-06-02		9810176	0.557	0.028	0.199	0.022	0.055	0.008	0.309	0.110	29.62
453	Tea	2004-06-02		9809920	1.572	0.079	0.532	0.055	0.145	0.020	0.709	0.178	34.12
113	Amalthea	2004-06-04		9810432	2.371	0.119	0.878	0.091	0.244	0.034	0.997	0.227	40.77
623	Chimaera	2004-06-18		9935104	2.318	0.116	0.751	0.077	0.203	0.028	0.773	0.176	43.69
572	Rebekka	2004-06-19		9935360	0.820	0.041	0.296	0.033	0.082	0.012	0.337	0.115	40.55
273	Atropos	2004-06-22		9934848	1.672	0.084	0.468	0.049	0.123	0.017	0.698	0.162	29.20
623	Chimaera	2004-07-09		10085120	1.353	0.068	0.448	0.047	0.122	0.017	0.569	0.150	35.58
138	Tolosa	2004-07-09		10084864	5.888	0.294	2.144	0.218	0.595	0.080	2.197	0.449	45.01
234	Barbara	2004-07-29		11779328	2.735	0.137	0.818	0.085	0.217	0.030	0.825	0.183	43.82
376	Geometria	2004-08-23		11896576	2.291	0.115	0.803	0.082	0.221	0.030	0.814	0.193	45.12
376	Geometria	2004-08-24		11896832	2.278	0.114	0.706	0.072	0.189	0.026	0.483	0.181	65.06
364	Isara	2004-09-21		12058624	3.301	0.165	0.789	0.084	0.200	0.028	0.541	0.236	61.34
189	Phthia	2004-09-21		12058112	2.699	0.135	0.766	0.079	0.201	0.028	0.512	0.213	65.34
856	Backlunda	2004-10-14		12428544	2.642	0.132	0.769	0.080	0.203	0.028	0.867	0.254	38.95
364	Isara	2004-10-14		12232448	4.706	0.235	1.171	0.121	0.299	0.041	0.766	0.322	64.89
1137	Raissa	2004-10-14		12232960	1.215	0.061	0.388	0.041	0.105	0.015	0.524	0.138	33.18
60	Echo	2004-11-04		12393728	3.204	0.160	0.953	0.100	0.253	0.035	1.060	0.223	39.70
60	Echo-1	2004-11-04		12544000	3.285	0.164	1.064	0.109	0.288	0.039	1.116	0.241	42.88
60	Echo-2	2004-11-04		12544512	3.209	0.160	0.965	0.100	0.257	0.035	1.113	0.241	38.35
189	Phthia	2004-11-05		12393984	2.035	0.102	0.583	0.061	0.154	0.021	0.759	0.187	33.60

Table 3—Continued

#	Asteroid	Obs. Date	AORKEYS <sup>a</sup>		$F_{24}^b$	$err_{24}^b$	$F_{70}^b$	$err_{70}^b$	$P_{160}^b$	$err_{P160}^b$	MIPS160 <sup>c</sup>	$err_{M160}^c$	CF <sup>d</sup>
			24+70	160									
131	Vala	2004-11-29		12870656	1.364	0.068	0.361	0.040	0.093	0.014	0.409	0.114	37.94
198	Ampella	2004-12-02		12870144	2.823	0.141	0.881	0.091	0.236	0.032	0.860	0.186	45.67
198	Ampella	2005-01-02		13070336	4.228	0.211	1.379	0.141	0.374	0.051	1.270	0.270	48.89
470	Kilia	2005-01-02		13070848	1.764	0.088	0.581	0.060	0.158	0.022	0.593	0.203	44.20
248	Lameia	2005-01-02		13070592	3.040	0.152	0.907	0.094	0.241	0.033	1.311	0.305	30.56
376	Geometria	2005-01-24	13107456	13107200	1.391	0.070	0.452	0.048	0.122	0.017	0.593	0.137	34.29
556	Phyllis	2005-01-24	13107968	13107712	2.208	0.110	0.557	0.059	0.142	0.020	0.416	0.116	56.99
757	Portlandia	2005-01-29	13108480	13108224	2.932	0.147	0.958	0.099	0.260	0.035	0.887	0.193	48.65
443	Photographica	2005-03-01	13307648	13307392	1.525	0.076	0.467	0.050	0.125	0.018	0.241	0.212	86.22
495	Eulalia	2005-03-02	13308160	13307904	2.697	0.135	0.746	0.077	0.195	0.027	0.887	0.232	36.53
512	Taurinensis	2005-03-02	13307136	13306880	0.977	0.049	0.238	0.026	0.061	0.009	0.204	0.445	49.38
443	Photographica	2005-04-05	13443840	13443584	2.615	0.131	0.682	0.071	0.176	0.024	0.872	0.315	33.55
118	Peitho	2005-05-14	13637120	13636864	4.531	0.227	1.217	0.126	0.316	0.043	1.206	0.262	43.54
584	Semiramis	2005-05-14	13636608	13636352	2.578	0.129	0.805	0.084	0.216	0.030	1.141	0.257	31.47
435	Ella	2005-05-15	13637632	13637376	4.176	0.209	1.257	0.129	0.335	0.046	1.345	0.288	41.38
282	Clorinde	2005-06-18	15244800	15244544	3.021	0.151	0.824	0.087	0.215	0.030	0.840	0.193	42.50
126	Velleda	2005-06-18	15245824	15245568	3.969	0.198	0.976	0.101	0.248	0.034	1.194	0.257	34.59
877	Walkure	2005-06-18	15245312	15245056	4.043	0.202	1.139	0.117	0.299	0.041	1.252	0.262	39.68

<sup>a</sup>Unique identifier for data in the Spitzer archive. Where only the 160 AORKEY is given, the same key applies to the 24 and 70  $\mu\text{m}$  data.

<sup>b</sup>Color-corrected flux densities and uncertainties in Jy. The uncertainties include the uncertainty in the absolute calibration of the 24 and 70  $\mu\text{m}$  bands (2% and 5%, respectively).

<sup>c</sup>Color-corrected 160  $\mu\text{m}$  channel flux density and uncertainty, in instrumental units.

<sup>d</sup>Calibration factor derived from each observation, MJy/sr/MIPS160.



Table 4. 70  $\mu\text{m}$  (Bright) Sample

#	Asteroid	Obs. Date	AORKEYS <sup>a</sup>						MIPS160 <sup>c</sup>	$err_{M160}^c$	CF <sup>d</sup>
			70	160	$F_{70}^b$	$err_{70}^b$	$P_{160}^b$	$err_{P160}^b$			
337	Devosa	2003-12-13		8780288	5.573	0.285	1.476	0.057	4.056	0.307	60.49
1584	Fuji	2003-12-13		8779520	0.478	0.025	0.127	0.057	0.603	0.063	34.90
752	Sulamitis	2003-12-13		8780032	0.654	0.040	0.173	0.066	0.624	0.074	46.14
198	Ampella	2004-01-25		8811776	2.667	0.144	0.706	0.060	2.585	0.108	45.43
83	Beatrix	2004-01-25		8812032	3.384	0.182	0.896	0.059	3.830	0.142	38.90
345	Tercidina	2004-01-25		8812288	4.336	0.233	1.149	0.059	4.913	0.232	38.85
25	Phocaea	2004-02-23		9065472	1.425	0.087	0.378	0.066	1.342	0.199	46.77
345	Tercidina	2004-02-23		9065984	6.478	0.338	1.716	0.058	6.106	0.216	46.71
783	Nora	2004-03-18		9194240	0.996	0.056	0.264	0.062	1.641	0.441	26.72
60	Echo	2004-06-01		9809408	1.458	0.078	0.386	0.059	1.192	0.132	53.85
18	Melpomene	2004-06-18		9934592	5.618	0.290	1.488	0.057	5.069	0.173	48.79
7	Iris	2004-06-20		9934080	14.209	0.732	3.764	0.057	13.010	0.244	48.08
505	Cava	2004-07-11		10084608	4.834	0.258	1.280	0.059	4.842	0.167	43.95
40	Harmonia	2004-07-11		10084352	7.618	0.396	2.018	0.058	7.084	0.143	47.35
40	Harmonia	2004-07-29		11779840	10.392	0.536	2.753	0.057	9.792	0.225	46.72
20	Massalia	2004-07-29		11778816	6.575	0.338	1.742	0.057	6.406	0.153	45.18
40	Harmonia	2004-08-23		11896064	13.304	0.683	3.524	0.057	12.246	0.202	47.83
20	Massalia	2004-08-23		11895552	5.503	0.284	1.458	0.057	5.885	0.171	41.16
19	Fortuna	2004-09-15		12057600	12.648	0.646	3.351	0.057	20.179	0.677	27.60
12	Victoria	2004-09-22		12057088	3.295	0.176	0.873	0.059	7.575	2.197	19.15
3	Juno	2004-09-26		12059648	21.511	1.107	5.698	0.057	33.718	2.360	28.09
12	Victoria	2004-10-14		12231936	4.941	0.256	1.309	0.058	5.977	0.437	36.39
313	Chaldaeaa	2004-11-04		12393216	1.582	0.086	0.419	0.060	2.167	0.156	32.14
12	Victoria	2004-11-04		12392704	5.369	0.275	1.422	0.057	9.404	0.938	25.14
433	Eros	2004-11-29		12869120	2.212	0.115	0.586	0.058	2.069	0.104	47.09
83	Beatrix	2005-01-02		13071360	6.339	0.328	1.679	0.058	5.682	0.152	49.12
433	Eros	2005-01-02		13071104	3.578	0.185	0.948	0.058	3.070	0.116	51.31
21	Lutetia	2005-01-24	13106944	13106688	7.806	0.401	2.068	0.057	7.566	0.184	45.42
12	Victoria	2005-03-02	13306624	13306368	3.497	0.193	0.926	0.061	4.342	0.334	35.46
7	Iris	2005-04-12	13442304	13442048	13.522	0.700	3.582	0.058	18.829	1.420	31.62
42	Isis	2005-05-16	13636096	13635840	11.057	0.567	2.929	0.057	8.648	0.174	56.29
6	Hebe	2005-06-18	15244288	15244032	13.356	0.685	3.538	0.057	11.163	0.208	52.67
471	Papagena <sup>e</sup>	2005-07-27	15418112	15417856	10.433	0.535	2.764	0.057	10.070	0.188	45.61
471	Papagena <sup>e</sup>	2005-07-27	15418624	15418368	12.347	0.634	3.271	0.057	10.317	0.163	52.69
471	Papagena <sup>e</sup>	2005-07-27	15419136	15418880	11.598	0.595	3.072	0.057	10.002	0.171	51.05
23	Thalia <sup>e</sup>	2005-07-28	15419648	15419392	2.914	0.152	0.772	0.058	2.987	0.143	42.94
23	Thalia <sup>e</sup>	2005-07-28	15420160	15419904	3.283	0.172	0.870	0.058	2.897	0.138	49.88
23	Thalia <sup>e</sup>	2005-07-28	15420672	15420416	3.122	0.163	0.827	0.058	3.327	0.099	41.30
313	Chaldaeaa	2005-08-26	15813632	15813376	4.613	0.238	1.222	0.057	5.761	0.290	35.26
41	Daphne	2005-08-27	15813120	15812864	7.544	0.388	1.999	0.057	7.634	0.184	43.51
138	Tolosa	2005-08-29	15814656	15814400	2.023	0.108	0.536	0.059	2.035	0.106	43.78
433	Eros	2005-09-04	15814144	15813888	0.509	0.032	0.135	0.068	0.968	0.308	23.18
42	Isis <sup>e</sup>	2005-11-09	16259584	16258816	10.474	0.537	2.775	0.057	9.879	0.168	46.68
42	Isis <sup>e</sup>	2005-11-09	16259840	16259072	12.191	0.624	3.229	0.057	9.869	0.199	54.38

Table 4—Continued

#	Asteroid	Obs. Date	AORKEYS <sup>a</sup>		$F_{70}^b$	$err_{70}^b$	$P_{160}^b$	$err_{P160}^b$	MIPS160 <sup>c</sup>	$err_{M160}^c$	CF <sup>d</sup>
			70	160							
42	Isis <sup>e</sup>	2005-11-09	16260096	16259328	9.367	0.480	2.481	0.057	8.428	0.218	48.93
20	Massalia <sup>e</sup>	2005-11-30	16465408	16464384	9.298	0.478	2.463	0.057	8.222	0.144	49.78
20	Massalia <sup>e</sup>	2005-11-30	16465664	16464640	8.073	0.415	2.138	0.057	6.768	0.148	52.51
20	Massalia <sup>e</sup>	2005-11-30	16465920	16464896	9.324	0.478	2.470	0.057	8.452	0.188	48.57
20	Massalia <sup>e</sup>	2005-11-30	16466176	16465152	7.104	0.366	1.882	0.057	7.140	0.166	43.81
85	Io	2006-01-11	16617984	16617728	5.520	0.286	1.462	0.058	5.973	0.148	40.69
51	Nemausa	2006-01-12	16618496	16618240	9.987	0.511	2.645	0.057	9.389	0.210	46.83

<sup>a</sup>Inique identifier for data in the Spitzer archive. Where only the 160 AORKEY is given, the same key applies to the 70  $\mu\text{m}$  data.

<sup>b</sup>Color-corrected flux densities and uncertainties in Jy. The uncertainties include the uncertainty in the absolute calibration of the 24 and 70  $\mu\text{m}$  bands (2% and 5%, respectively).

<sup>c</sup>Color-corrected 160  $\mu\text{m}$  channel flux density and uncertainty, in instrumental units.

<sup>d</sup>Calibration factor derived from each observation, MJy/sr/MIPS160.

<sup>e</sup>These objects were observed several times on the given date. The Papagena and Thalia observations were taken without interruption; those for Isis and Massalia were spaced by about 2 hours. Lightcurve variations caused by the shape of these targets are predicted to contribute about 5% to the observed variation except for all except Papagena, where the lightcurve should have only contributed about a 1% variation over the observing interval.